An equilibrium-based design workflow for Member Structural System integrating Combinatorial Equilibrium Modelling, Vector-based Graphic Statics, and Material concretization

Abstract: This paper presents an equilibrium-based method for designing member-based structural systems, which fulfills the objectives of form generation, shape optimization, and materialization. It leverages and refines three algorithms: Combinatorial Equilibrium Modelling (CEM), Vector-based Graphic Statics (VGS), and a customized materialization method. These algorithms are integrated into a workflow that commences with a modified CEM for a minimized load path form-finding within a constrained domain. The model is then transformed through VGS in a dynamic process for subjective design purposes. Finally, the material concretization method specifies and dimensions the optimized strut-and-tie model. The paper describes the initiation and termination conditions for each step. Two case studies, a virtual truss bridge and a detailed wooden tower, demonstrate the method, highlighting the merit of this interactive workflow in bridging the gap between structural engineers and architects.

Keywords: member structural system, integrated workflow, combinatorial equilibrium modelling, vector-based graphic statics, material concretization.

1. Introduction

1.1 Interactive design using Graphic Statics

Graphic Statics is an equilibrium-based design and analysis method particularly suited for pin-jointed planar or spatial networks. It relies on geometrical rather than numerical operations between its reciprocal form and force diagrams. Originating in the 16th century, Graphic Statics was formulated as a scientific discipline in the 19th Century, especially by Rankine (1858, 1864), Culmann (1864), Maxwell (1864, 1870), Bow (1873), and Cremona (1890). It was of use for more than a century before gradually disappearing from civil engineering practice during the 20th century as a consequence of the development of computer science and numerical calculation (Waclaw & Edward, 1998). Fortunately, a recent revival of graphic statics in a CAD environment has enabled dynamic interaction between form and force diagrams with real-time feedback (Van et al. 2012).

1.2 Development of 3D Graphic Statics

Among various current developments in Graphic Statics, the polyhedral and vector approaches have continued to make progress over the last few years (Lee, 2018). The polyhedral approach represents force diagrams as an assembly of polyhedral cells, introduced by Rankine in 1864, whose seminal work on the topic was only a half-page long. The polyhedral force-form reciprocal relationship is also referred to as “Rankine reciprocal” (Konstantatou et al., 2018). Akbarzadeh applied and extended Rankine’s theories graphically through a 3D computational framework, in which the area and orientation of faces in the polyhedral cell represent the direction and magnitude of forces in the corresponding member (Akbarzadeh, 2016). Polyframe2 (Lu et al., 2024) and Compas_3gs (Lee, 2018) are currently two developed digital design tools based on Polyhedral Graphic Statics, which utilize multi-cell polyhedra and disjointed cell networks to perform constrained geometry operations, changing or generating new structural forms (Akbarzadeh et al., 2015). Hence, the form-finding operation process was unfriendly to

designers who had limited knowledge of graphic statics. The difficulty lies in discerning a specific polyhedron from cell clutter or determining the type of geometry operation that can be executed.

As for the vector approach, it considers a force diagram consisting of closed cycles of force vectors, which is also referred to as the "Cremona reciprocal" (Crapo, 1979). In this approach, the vector length corresponds to the magnitude of the force, and the vector direction aligns with the direction of the force. However, it is not possible to assemble a force diagram of a 3D spatial network without having duplicate or "non-overlapping" edges through the vector approach (Jasienski et al., 2024). Although vector-based 3D form-force diagrams exhibit imperfect duality, their use of arrowed lines significantly simplifies the geometric operation process for users. Maxwell (1864) also noted that it is always possible to construct force diagrams with vectors representing the forces acting on a structure in static equilibrium. VGS (Vector-based Graphic Statics) and CEM (Combinatorial Equilibrium Modelling), currently two digital vector-based design tools, respectively undertake structural design and form-finding tasks during the conceptual design phase. CEM performs structural form-finding through topological diagrams and metric variations, delivering a corresponding pin-jointed spatial network defined by prestressed compression or tension bars (Ohlbrock et al., 2016, 2020). VGS generates vector-based force diagrams and utilizes particle-spring systems embedded in Kangaroo2 (Piker, 2013) to conduct various transformation goals while the structure form remains in an equilibrium state (Fivet, 2016; D'Acunto et al., 2019). Both CEM and VGS are also based on the lower-bound theorem of plasticity, which means they produce structural forms of comparable efficiency (Aurelio Muttoni et al., 1997). The integration of these two approaches unlocks tremendous potential for innovative structural design.

1.3 Structure Design of Bar-Member Systems

Currently, the design of Member-based Structural Systems has shifted to more integrated, performance-driven, and computationally advanced approaches. Among them, Finite Element Analysis (FEA) allows engineers to simulate intricate geometries and nonlinear behaviors with high accuracy. Structural Optimization involves adjusting the cross-sectional dimensions, modifying the overall geometry, and determining the efficient layout of material within a bar system. Parametric Design uses algorithms to automatically generate and evaluate thousands of design variations based on a set of constraints. Both powerful techniques allow for a rapid exploration of the design space to find high-performing and architecturally interesting solutions. Nevertheless, a significant limitation of these methodologies is that their outputs are typically optimized for a singular, predefined objective, which precludes the designer from directly and intuitively investigating the dynamic interplay between form and force. This underscores the significance of digitalized tools for Vector-based Graphic Statics. However, the geometric models generated by CEM and VGS frameworks cannot address the issues of material realization. Additionally, another problem to be solved in this research is how to integrate these two frameworks and define their initial and terminal conditions.

1.4 Research objective

To facilitate a member-based structural design strategy from lower and higher fidelity (geometrical and physical). This research presents a bespoke design workflow that integrates CEM, an equilibrium-based form-finding tool; VGS, a structural design and optimization tool; and Material concretization, a self-defined dimensioning algorithm. The contribution of this research is detailed below:

1. An equilibrium spatial structural geometry with minimized load paths by automatically tuning input

trail lengths and deviating forces.

2. An integrated workflow that allows designers to manipulate force and form for a member-based structure system interactively.

3. A dimensioned physical structure model considering material property and buckling issue to guarantee the viability of the generated geometry model (Figure 1).

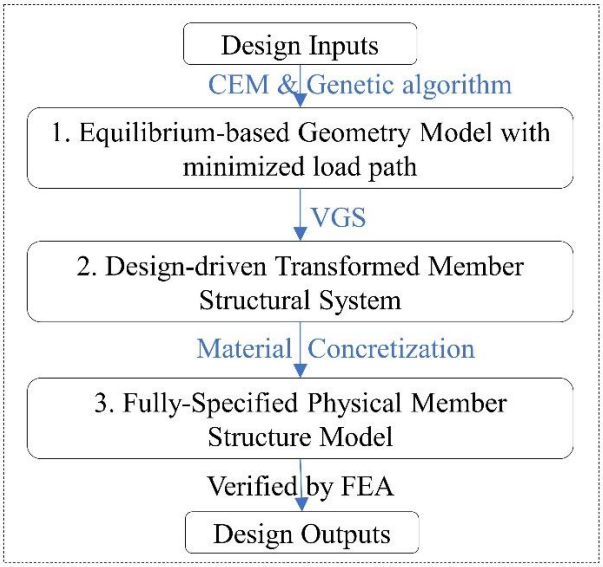


Figure 1: Design objective at each step

1.5 Content and Nomenclature

Following the introduction in Section 1, Section 2 outlines the principle of the workflow for each step. Section 3 exemplifies a virtual bridge and a real tower design case to prove the feasibility of this design method. The final section highlights the shortcomings in current research and proposes directions for the future. In this article, the form and force diagrams are referred to as $\boldsymbol{F}$ and $\boldsymbol{F}^*$, respectively. The nomenclature for representing individual elements of the diagram is listed in Table 1.

Nomenclature		
Class	Implication	Symbol
CEM	Topology diagram	$\mathbf{T}$
	The sequence of the topology graph	k
	Trail length in sequence k	t_k
	Deviation of the member's force magnitude in sequence k	d_k
	Numeric value of threshold	ε
	The unknown position vector in sequence k	$\boldsymbol{P_k}$
	Position vector at iteration j	$\mathbf{P_j}$
	External force vectors	$\boldsymbol{q^*}$
	External force vectors in sequence k	$\boldsymbol{q^*_k}$
	Deviation force vectors in sequence k	$\boldsymbol{D^*_k}$
	Indirect deviation force vectors in sequence k	$\boldsymbol{I^*_k}$
	Trail force vector in sequence k	$\boldsymbol{f^*_k}$
	The j-th individual force vector acting on node i	$\boldsymbol{F_{j,i}}$

VGS	Planar graph	$\boldsymbol{T_P}$
	Force Diagram	$\boldsymbol{F^*}$
	Form Diagram	$\boldsymbol{F}$
	The residual nodal vector	$\mathbf{R_i}$
	The external load vector	$\mathbf{Q_j}$
Material concretization	Cross-sectional area	A
	Axial forces	N
	Critical tension stress	σ_t
	Critical buckling stress	σ_{cr}
	Material's tension strength	f_t
	Material's compressive strength	f_c
	Effective length factor	μ
	Length of bar member	L
	Radius of gyration	r
	Slenderness Ratio	λ
	Critical Slenderness Ratio	λ_c
	Cross-sectional moment of inertia	I
	Elasticity module	E

Table 1: Nomenclature table

2. Methodology Statement

2.1 Integrated structure design workflow

Figure 2 illustrates this framework. A user-defined topology diagram with an appropriate geometric configuration and metric setting initiates it. An equilibrated spatial network shall be generated by varying the tuning parameters in CEM. Then, a global or local transformation could be applied to the system with different optimization goals. Lastly, the transformed geometry model is used with the material concretization procedure to determine the appropriate sectional size. A detailed finite element analysis using Karamba3D was conducted to verify the practicality of the workflow. In most cases, the spatial network generated through CEM is only optimized for specified external loading conditions. To adapt such spatial networks to arbitrary loading scenarios, corresponding bracing systems can also be incorporated into the system to formulate a geometrically stable structure. Leveraging the “Evaluate Equilibrium” component in VGS may output the static and kinematic determinacy of the spatial network to indicate if a member should be added (Calladine & Pellegrino, 1991; Micheletti, 2008).

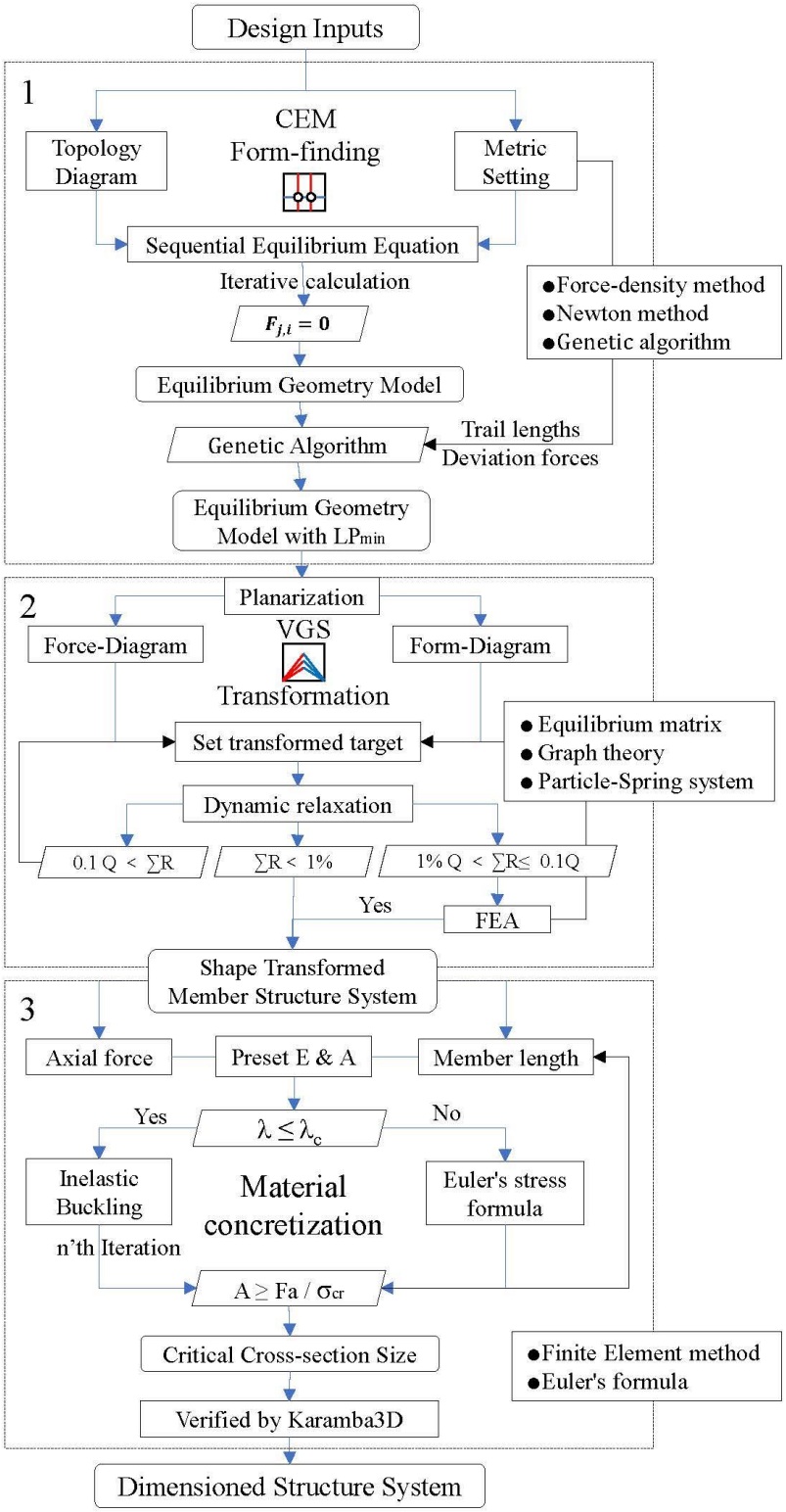


Figure 2: Framework of the integrated workflow

2.2 Form-finding and optimization with CEM and Genetic Algorithm

To initiate the form-finding process, a topology diagram **T**, comprising two distinct members, must be predefined in CEM. Members from external load-applied points to support points are called trails; members connecting these trails in the same or different sequence are called deviations. Trail's length *t*,

deviation's force magnitude *d*, and original node position p are predefined by users. For a given $\boldsymbol{T}$ with *K* sequences, under external load vectors $\boldsymbol{q}^*_k$, the unknown position vector $\boldsymbol{P}_{k+1}$ in sequence *K+1* can be obtained through nodal equilibrium:

$$\boldsymbol{f}^*_{k+1} = -\boldsymbol{f}^*_k - \boldsymbol{D}^*_k - \boldsymbol{q}^*_k \tag{1}$$

$$\boldsymbol{P}_{k+1} = \boldsymbol{P}_k + t_{k+1} \cdot \boldsymbol{f}^*_{k+1} / |\boldsymbol{f}^*_{k+1}| \tag{2}$$

Where $\mathbf{f}^*_\mathbf{k}$, $\mathbf{D}^*_\mathbf{k}$ are the trail and deviation force vectors in sequence K, t_{k+1} is the trail length in sequence K+1. While indirect deviation members connect nodes in different sequences in the topology graph $\boldsymbol{T}$, Equation (2) should be modified as:

$$\boldsymbol{f}^*_{k+1} = -\boldsymbol{f}^*_k - \boldsymbol{D}^*_k - \boldsymbol{q}^*_k - \boldsymbol{I}^*_k \tag{3}$$

$\boldsymbol{I}^*_k$ refers to the indirect deviation force vectors in sequence K. The solution of equation (3) employs an iterative method, where the sum of the differences between all nodal vector positions in one iteration and the next is smaller than a given threshold (Saad, 2003).

$$\sum |\boldsymbol{P}_{j+1} - \boldsymbol{P}_j| \leqslant \varepsilon \tag{4}$$

The form-finding process is concluded. Static equilibrium is achieved when there are zero resultant forces at all nodes (Figure 3-4).

$$\sum_j \boldsymbol{F}_{j,i} = \mathbf{0} \tag{5}$$

where $\boldsymbol{F}_{j,i}$ is the j-th individual force vector acting on node i.

During the form-finding process, different configurations of $\boldsymbol{T}$ introduce a spectrum of design spaces for varied objectives. $\boldsymbol{T}$ can be combinatorially adjusted with trail lengths and deviation forces, to achieve the desired form under given external loading conditions. For trail lengths, the sign determines the force property, which compression (negative) guides the trail down to the ground and tension (positive) leads the trail up to the sky. For deviation forces, under the condition of compressive trails, tensile deviation members would pull the trails inward, and compression deviation members would push the trails outward. It is worth noting that the process described above can be transformed into a non-chronological approach at any time. The input parameters can be carried out manually, automatically, or through a combined approach (Zongshuai et al., 2021).

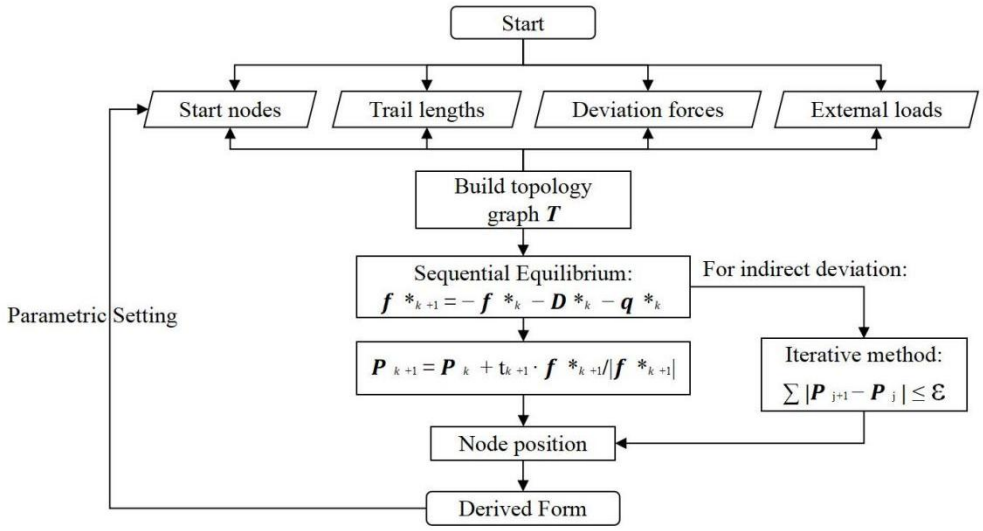


Figure 3: Form-finding roadmap in CEM

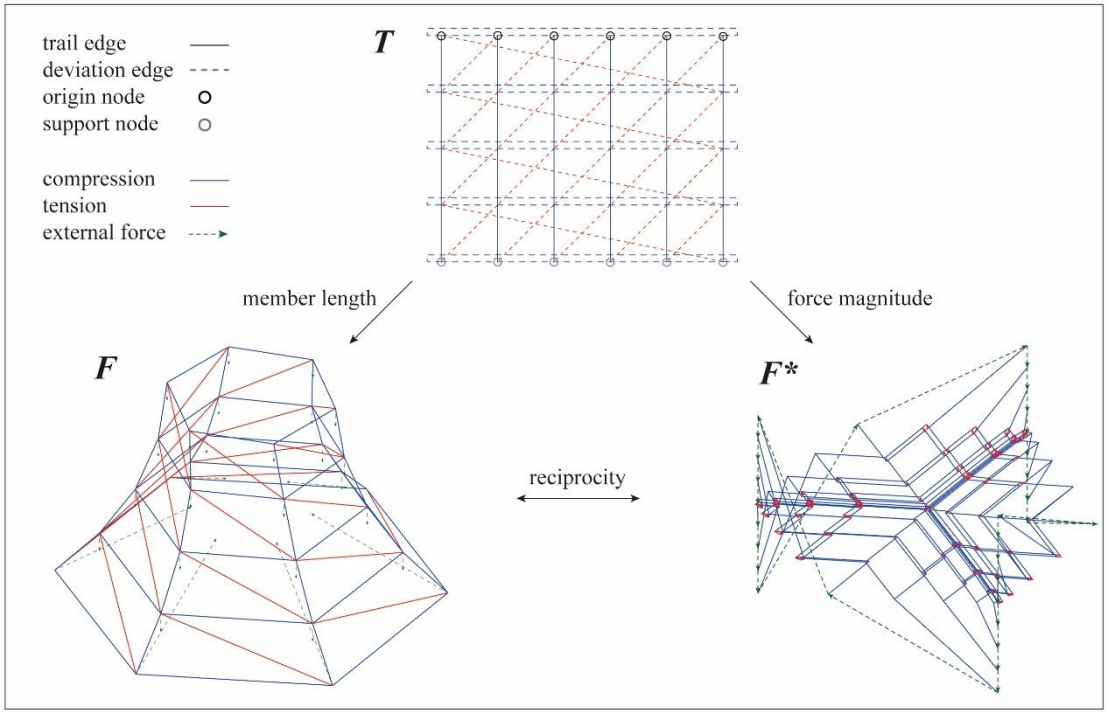


Figure 4: Geometric model generated by CEM (***T***: topology diagram, ***F***: form diagram, ***F****: force diagram, blue: compression member, red: tension member, green: external loading member).

To optimize the equilibrium spatial network generated by CEM. The Genetic Algorithm in Galapagos plugin within the Grasshopper platform was utilized to achieve a minimized Load Path form. Load Path is defined as the sum of the product of the absolute value of internal force and length for all members:

$$LP = \sum_{i=1}^{n} |F_i| \cdot L_i \tag{6}$$

In engineering practice, minimizing *LP* implies minimizing the material volume by creating the most direct flow of forces (Baker W.F. et al., 2012). The Genetic Algorithm in Galapagos begins with the creation of a random population of individuals to be tested against the Fitness Function. After testing a generation, the worst performers are removed, and the top performers are selected and paired up to create a new generation (Rutten D., 2013). To adapt the Galapagos Evolutionary Solver for the form-finding framework of CEM, this study implements three key adjustments. First, to prevent the generation of forms with excessively long members, a penalty factor *P* (a large number) and a quadratic term were introduced into the fitness function. If member lengths become excessive, the fitness value increases drastically, causing Galapagos to cull these genomes rapidly.

$$Fitness = LP + P \cdot (L - L_{limit})^2 \tag{7}$$

Second, continuously differentiable functions (such as parabolic equations) were employed to control the distribution of trail lengths and deviation forces. By reducing the optimization scope to just two or three parameters, both convergence speed and smoothness were significantly enhanced. Finally, to mitigate

the risk of local optima, three strategies were employed: constraining the input parameters within appropriate ranges, leveraging the stochastic nature of genetic algorithms by restarting the solver multiple times to verify result consistency, and increasing the Mutation Rate to force the algorithm into a broader exploration of the solution space.

Figure 5 presents the results of three distinct optimization scenarios. For each group, the image above displays the final converged structural morphology, while the image below shows the corresponding fitness convergence graph. The scatter plot illustrates the optimization process with a population size of 50 individuals per generation. The narrowing of the fitness range indicates the solution converging towards the global optimum.

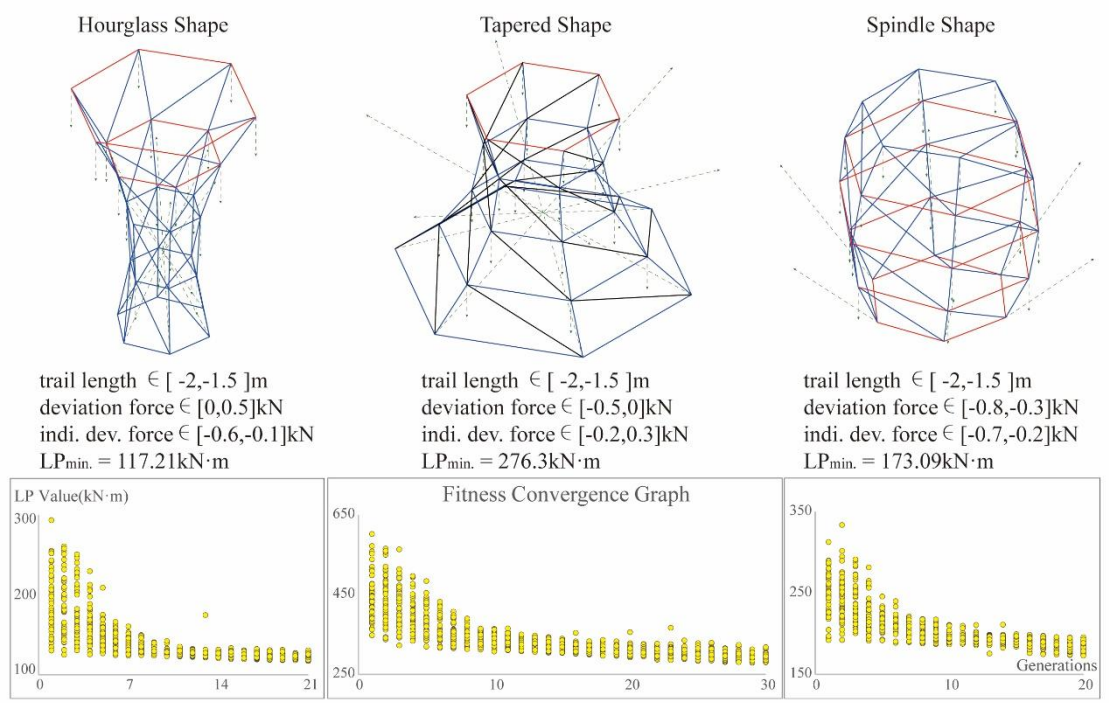


Figure 5: Optimization Results and Fitness Convergence (green line: external loads, blue line: compression members, red line: tension members, black line: zero members)

2.3 Reciprocal transformation in VGS

As the minimized load-path equilibrium spatial network is generated, the designer can fetch the external and internal force vectors and deliver them to VGS. VGS reassembled this spatial network to generate the reciprocal form and force diagram based on the embedded graph planarization and cycle construction algorithm. Whitney (1933) and Tutte (1963) noted that the planar graph serves as the basis for reciprocity between two diagrams. The automated graph planarization algorithm in VGS relies on a two-step process. It starts with a maximal planar subgraph, and the remaining edges are then successively added to this sub-planar graph. The planarization proceeds by sequentially adding new auxiliary vertices where the remaining edge crossed a sub-planar graph (Jasienski et al., 2024). Figure 6 illustrates the process. Once

a planar graph is generated, all the edges and vertices are categorized and stored in a list of lists, where each list represents a vertex and its connecting edges that can be used to assemble the closed cycle of its force vectors. These closed cycles are then assembled into a force diagram according to the node adjacency relationship of a planarized graph (D'Acunto et al., 2017).

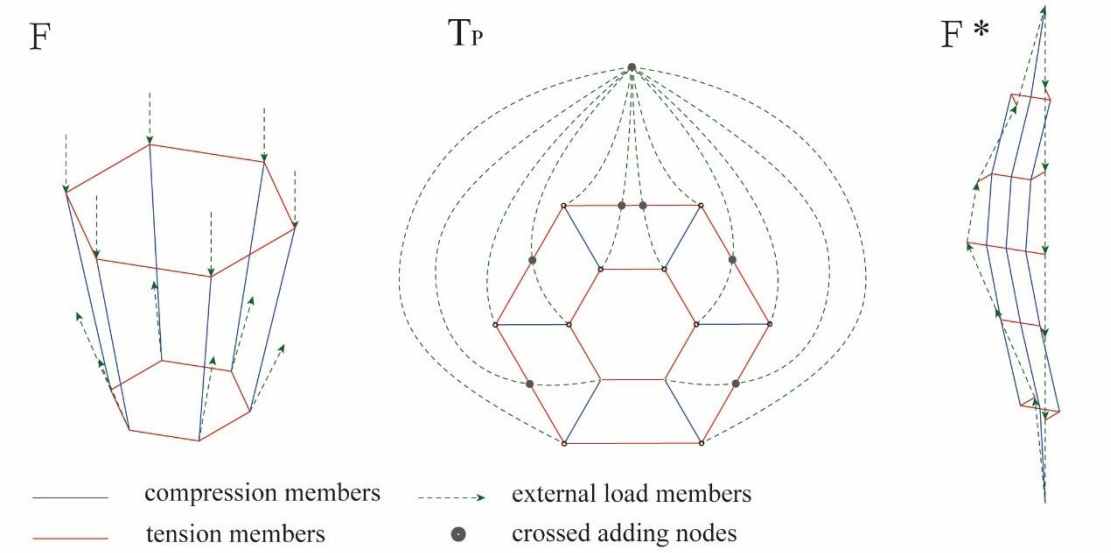


Figure 6: Planarization process in VGS (F: form diagram, F*: force diagram, T_P: Planarized graph).

Once the force-form diagram is established, constrained global and local transformations can be performed in VGS using the Kangaroo2 library to set different transformed goals. Since the algorithm embedded in *Kangaroo2* utilizes a particle-spring system to project the original form onto objectives and iterates to the equilibrium state in an oscillating process (Kilian & Ochsendorf, 2005; Barnes, 1999). Errors are inevitably introduced. To control errors in the transformation process, Oakley and Knight (1995) precisely defined the convergence criterion as a "relative error of the force imbalance" compared to the external static load vectors. Veenendaal and Block (2012) pointed out that this relative criterion can be relaxed to 1% to facilitate rapid iteration towards the desired state. In this study, given that the transformation is based on an equilibrium model, the 1% criterion appears to restrict the potential for transformation. This relative criterion is quantified by the ratio of two critical variables: the sum of norms of the i-th nodal residual vector, $\boldsymbol{R_i}$, and the sum of norms of the j-th nodal external load vector, $\boldsymbol{Q_j}$.

To specify the termination condition, an experiment featuring an escalating complexity in the transformation objectives was conducted on a spatial network generated by CEM (Figure 7). During the process, the sum of the nodal residual force vector norms increases with the complexity of the optimization target (Figure 8). The orange line (the sum of all post-transform nodal residual vector norms), which is 4.7% of the total magnitudes of its external loads, breaches the green line (1% of the total magnitudes of its external loads) in the final step. To verify the validity of the deformed structural model, it was imported into Karamba3D for finite element analysis under the same external load and support conditions as those in VGS. The results showed a displacement of only 3.73 mm, which is within an acceptable range compared to the model's size. Therefore, this study proposes a criterion that:

If $$\sum_i |\boldsymbol{R_i}| \leq 0.01 \sum_j |\boldsymbol{Q_j}| \quad (8)$$

The result of the shape transformation in VGS is considered valid.

If $$0.01 \sum_j |\boldsymbol{Q_j}| < \sum_i |\boldsymbol{R_i}| \leq 0.1 \sum_j |\boldsymbol{Q_j}| \quad (9)$$

The result must be validated using the FEM to demonstrate a reasonable range of displacement distribution.

If $$0.1 \sum_j |\boldsymbol{Q_j}| < \sum_i |\boldsymbol{R_i}| \quad (10)$$

The result is not accepted since the deviation of internal forces is considered too large, and it is necessary to reset the objectives or return to the first step (CEM) for another form-finding process.

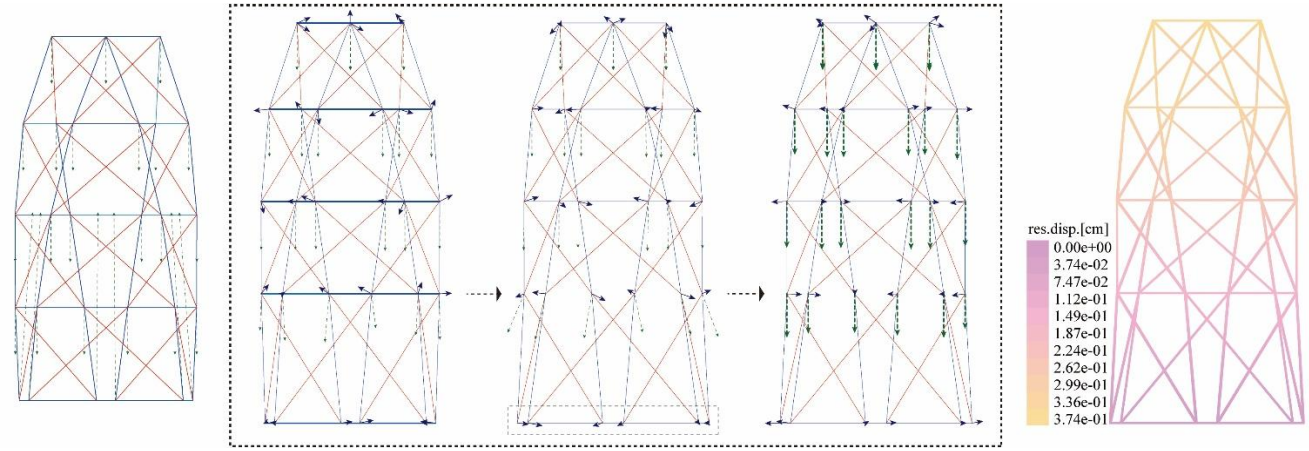


Figure 7: Transform experiments (left: original form, middle: three transformation strategies from simple to complex, right: verified by Karanmba3D) (blue: compression member, red: tension member, green: external loading member, dark blue: residual force vector).

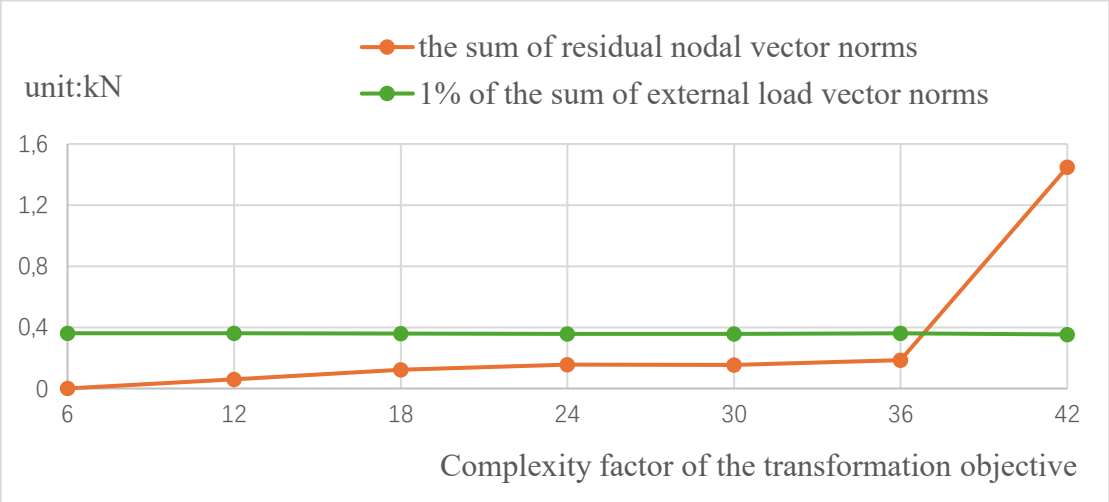


Figure 8: Line graph between the complexity of the transformation objective and the norms of the residual nodal and external load vectors.

2.4 Material concretization

The final step of this workflow proposes a series of modified formulas to determine the cross-sectional size and material properties of the spatial network represented by hinged red (tension)-blue (compression)-white (zero-member) bar systems. Firstly, each member's cross-sectional area A shall not be less than:

$$A \geq N/\sigma_t,\ A \geq N/\sigma_{cr} \tag{11}$$

Where N represents axial force, σ_t and σ_{cr} respectively represent the critical tension and buckling stress. For a real-world compression member, not only elastic buckling but also inelastic crushing should be considered. Therefore, design codes such as Chinese GB 50017, Eurocode 3, or American AISC provide a "Column Buckling Graph" based on extensive experiments and theoretical modifications. The Johnson Parabolic Formula (James Gere and Barry J. Goodno, 2016), which serves as the conceptual basis for the AISC column graph, is employed here to determine the critical buckling stress. It states that for short to intermediate columns, a parabolic curve is used to model inelastic buckling. For long and slender columns, it reverts to the original Euler formula for elastic buckling. The critical buckling stress σ_{cr} is defined as:

For Intermediate Compression bar (Inelastic Buckling, $\lambda \leqslant \lambda_c$),

$$\sigma_{cr} = f_c \cdot [1 - (f_c \cdot \lambda^2) / (4\pi^2 E)] \tag{12}$$

For Long Compression bar (Elastic Buckling, $\lambda > \lambda_c$),

$$\sigma_{cr} = \pi^2 E / \lambda^2 \text{ (standard Euler's stress formula)} \tag{13}$$

where f_c is the material's compressive strength (the yield strength for steel or the allowable compression stress for timber), E is the modulus of elasticity of the material, λ is the slenderness ratio, and λ_c is the critical slenderness ratio that marks the transition point where the parabolic formula and the Euler formula meet. λ and λ_c are defined by the formula expressed as:

$$\lambda = \mu L/r,\ \lambda_c = \pi\,(2E/f_c)^{1/2} \tag{14}$$

where μ is the effective length factor that characterizes the bar member's end restraint conditions. If the bar members' both ends are pin-jointed, μ equals 1. If both ends are fixed, μ equals 0.5. Considering different connection situations, a 10% to 20% upward adjustment of μ is needed. L represents the member length, and r represents the radius of gyration, which has a relationship with the cross-sectional moment of inertia I:

$$r = (I/A)^{1/2} \tag{15}$$

Through an appropriate calculation sequence based on equation (11-15), the cross-sectional dimensions of the strut-tie model will be iteratively determined. Firstly, the designer has to preset a cross-sectional area and determine a suitable material with its corresponding modulus. Secondly, calculate the slenderness ratio λ, its length, and the radius of gyration. Thirdly, calculate the critical buckling stress σ_{cr} for compression members. Lastly, compare if the preset cross-sectional area is satisfied (11). If so, reduce the preset area until equation (11) is no longer met. The critical cross-sectional area is achieved at the (n-1) th iteration. If the condition is not satisfied, increase the preset area until equation (11) is met, the critical area is achieved at the n'th iteration.

To verify this method, a dimensioning process was conducted on the spatial network transformed by VGS. Firstly, a timber species was selected to determine the elastic modulus, allowable compressive stress, and self-weight. Secondly, member lengths and axial forces were extracted from the VGS. Since the structure is a pin-jointed system, an effective length factor of 1.1 was adopted. Then, the preset cross-section dimensions were iteratively calculated following the above steps. Finally, it was concluded that the critical dimensions of cross-section 7×7 cm is the minimal integer solution. To validate the reliability of the result, Karamba3D, a parametric engineering tool in Grasshopper, was adopted due to its operational efficiency and accessibility. Import the geometrical model, apply the same external loads and boundary conditions, input the selected hardwood's elasticity modulus, and the calculated dimension to Karamba3D. Then, using the algorithms for evaluating buckling modes, as shown in Figure 9, the maximum displacement was found to be only 3.96mm.

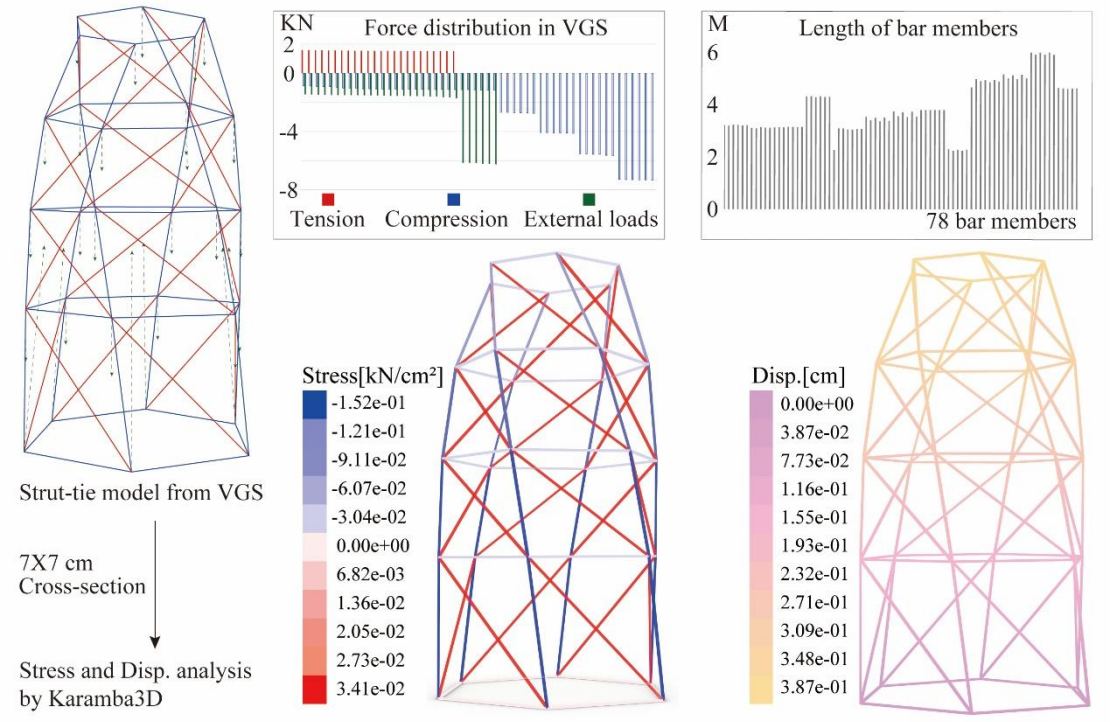


Figure 9: Stress and displacement verified by Karamba3D

3. Design application

3.1 Truss bridge

To verify the universality of this workflow, a design process for truss bridges was formulated. The initial topology diagram consisted of eight trial lines divided into two groups, fourteen rectangular rings connecting the tails in seven topological sequences, and four deviation members linking the starting nodes of the two tail groups. Vertical loads are applied to each node of the diagram, except for eight supports, and eight horizontal loads are exerted on each of the four starting nodes in opposite directions. Pre-added zero-axial force bracing members to the topological diagram were incorporated to eliminate the need for manual addition later.

With varying metric settings, three different truss bridges were generated from a single topology diagram. The force in deviation members, connecting the two groups of upper trails, was used to modify the width of the bridge deck. The greater the compression, the more expansive the bridge deck. The arch's rise was deepened by applying higher vertical loads to the nodes on the lower trails. Moreover, the length of the trails substantially influenced the bridge span. Figure 10 depicts the force distribution and morphological composition of the broader, deeper, and longer truss bridges.

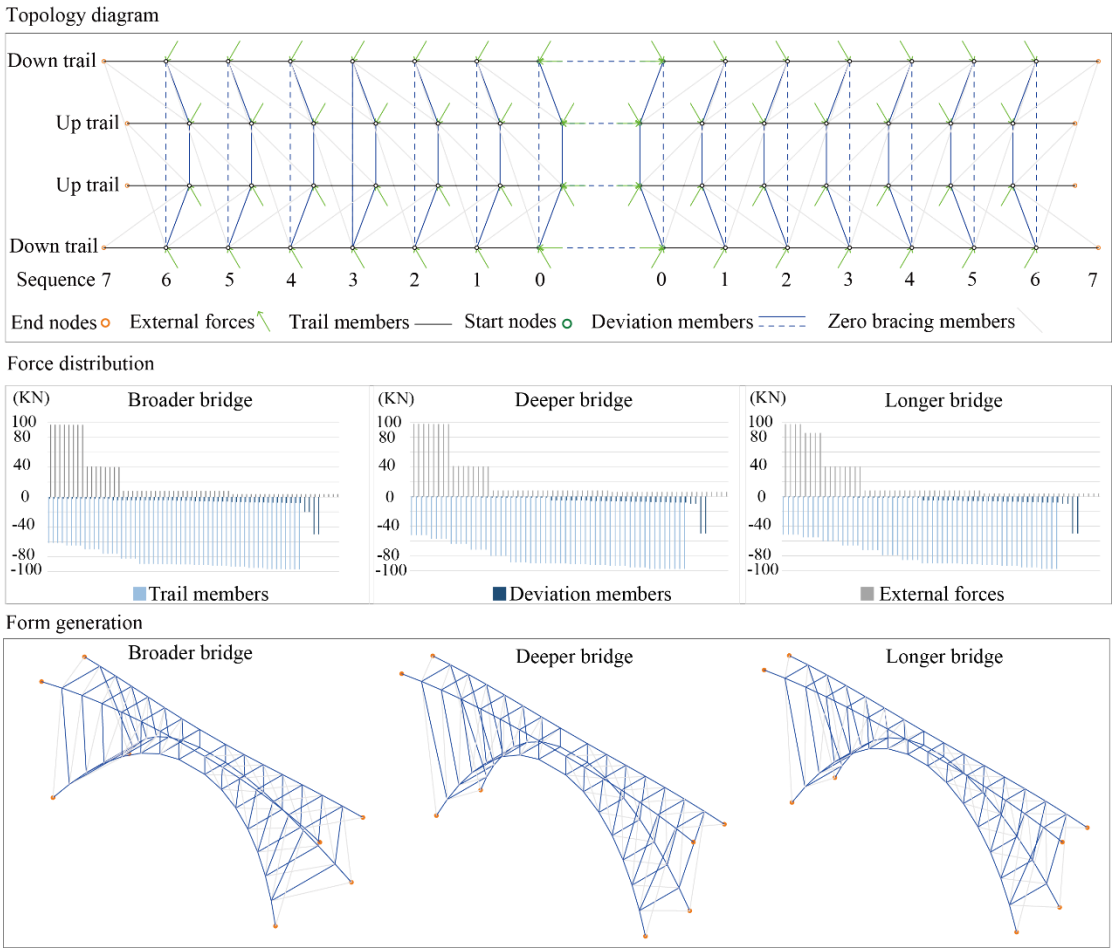


Figure 10: Three truss bridges generated by CEM

Through appropriate parameter adjusting, the final selected truss bridge schema was 2.1 meters in width, 8.0 meters in rise, and 35 meters in span. Then, a transformation process can be conducted through VGS. In this case, the nodes of the bridge deck are all constrained to a single plane while maintaining the direction and magnitude of all external load vectors. After 65 iterations, the sum of the residual vector norms reached 12.04, which fell within the range of 1% to 10% of the external loadings. Further finite element analysis verified that the structure's maximum displacement was only 2.04cm, indicating that the transformation process was successful (Figure 11). Lastly, the member length and axial force of the optimized truss bridge were extracted for cross-section dimensioning. Using the proposed material concretization method, a 10cm length and 0.2cm thickness steel square tube with an elastic modulus of 21000 kN/cm² was chosen as the preset data. After seven iterations, a critical sectional dimension output was 5.9cm in length with a thickness of 0.18cm. Verifying by Karamba3D, the inner stress and the maximum displacement are both within the permissible range.

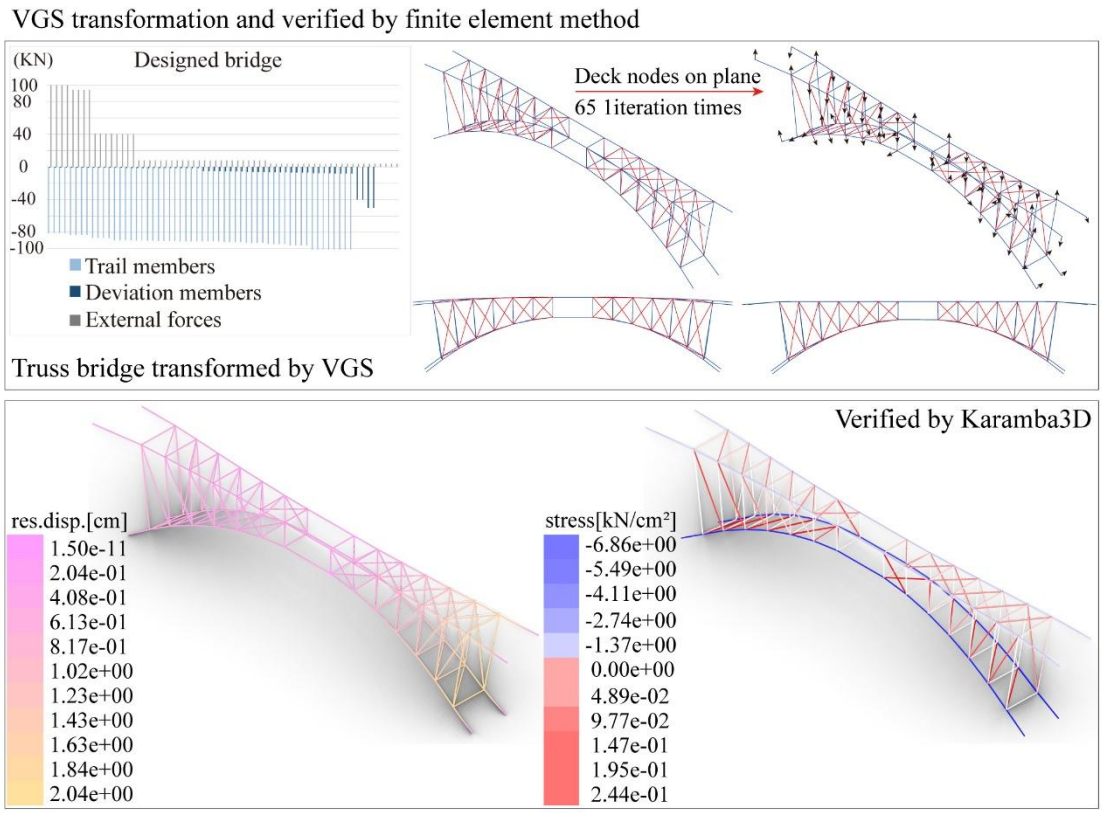


Figure 11: Transforming and verifying the results of the truss bridge

3.2 Timber tower

In addition to virtual design applications, a real wooden tower was designed and constructed during DigitalFutures 2024 at Tongji University in Shanghai. The tower scheme, initially inspired by the Sakyamuni Pagoda of Fogong Temple, which was constructed in 1056, is the oldest wooden multi-story structure in the world. From the exterior, the pagoda appears to have only five stories, yet its section reveals it has nine; the four hidden stories are added with diagonal bracing members in a radial direction to endow the building with good earthquake resistance properties (Figure 12).



Figure 12: The Sakyamuni Pagoda of Fogong Temple

Take this structural feature as a reference. The topology diagram built in CEM was confined to an orderly arrangement of trail lengths, specifically 2.7 and 0.6 meters, which constituted a rectangular prism where rectangular rings served as deviation members. Using the ‘Constraint Plane’ component in CEM, the

sequentially calculated node positions will always lie on the normal plane of the corresponding trail members in the topology diagram. As the vertical point loadings are uniformly applied, vectors of lateral force at each node could be used to find the desired structure shape. Figure 13 illustrates different results generated with verified lateral force vectors. Eventually, a fine-tuned twisted trail system with regularly distributed deviation rings in each layer was adopted as a preliminary scheme.

Three different transformation strategies were executed: The first aligned the direction of deviation members to varying degrees, specifically ± π /6, ±π/3, and ±π/2. The second constrained nodes of each story are at the heights of 0, 2.7, 3.3, 6.0, 6.6, and 9.3 meters—the third set deviation member's length on each layer. Since the results of the CEM are already sufficiently satisfying, with the sum of residual vector norms being less than the standard of 1%, the transformation effect is favorable. After the transformation, the bracing members were added between adjacent trails, thanks to spatially irregular and twisted morphology, a fortuitously statically and kinematically determinate 3D network (verified by VGS), thus built (Figure 14).

As the current core tube can resist arbitrary external loads, a more rigorous loading condition with a 2.0KN external point load is applied to the twisted tube. VGS calculates its inner axial forces and delivers them to the material concretization method. Table 2 lists the preset material properties used to determine the critical size of the cross-section as 8 × 8 cm. To verify this result, the same model was consolidated into 'Assemble Model' and connected to the 'Buckling Modes' component in Karamba3D. As the right side of Figure 14 indicates, the deformation that occurred at the top frame laterally slid only 2.21 cm. The analysis results confirm that the structure complies with the code of deformation requirements, and they also reveal the importance of limiting the lateral displacement of the rectangular deviation rings.

Material properties	
Tensile strength: 1.3 KN/cm^2	Young's modulus 1050 KN/cm^2
Compressive strength: -1.3 KN/cm^2	Specific weight: 6 KN/ m^3
Flow hypothesis: Rankine hypothesis	Shear modulus: 360 KN/cm^2

Table 2: Selected timber material properties

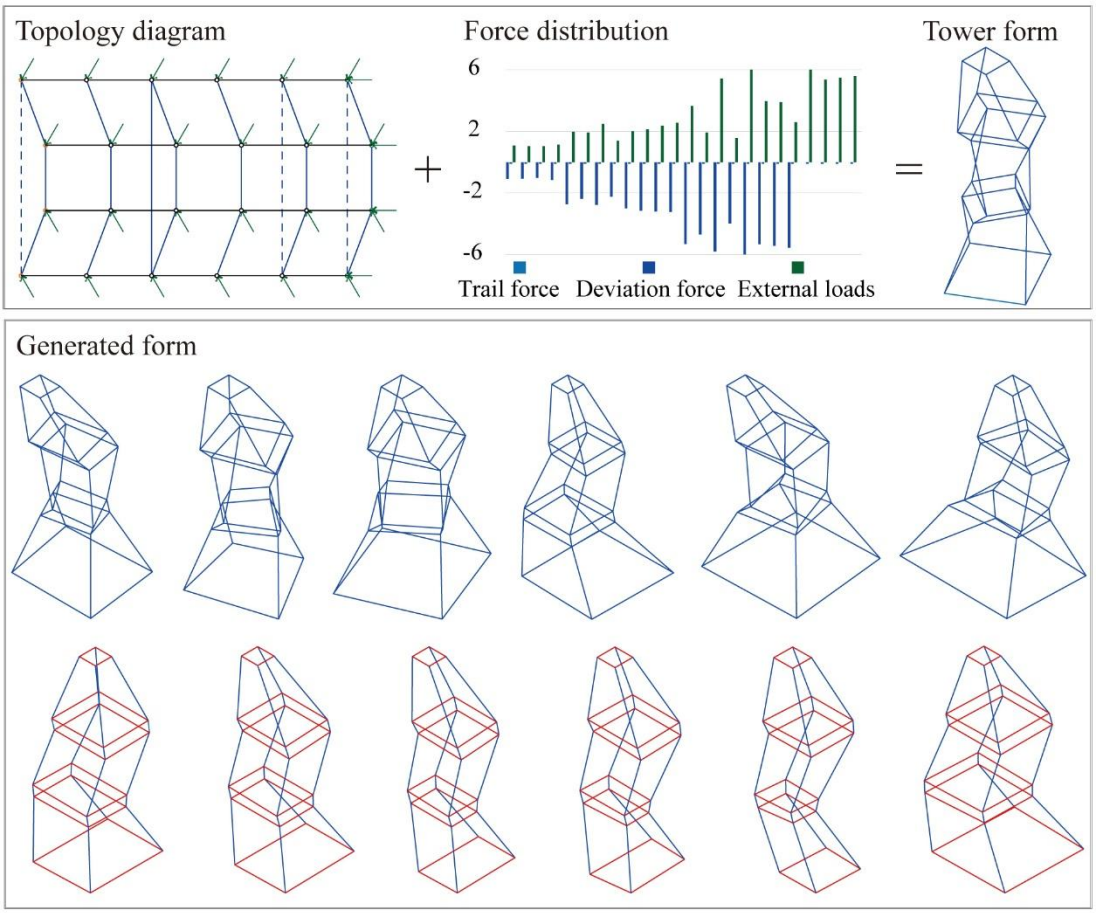


Figure 13: Different tube forms through CEM (Top is the chosen one)

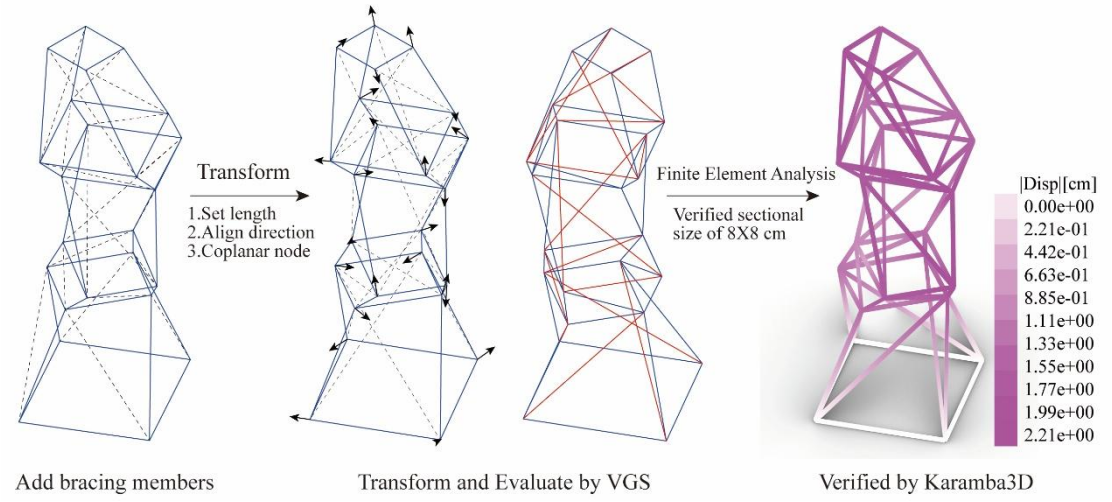


Figure 14: transformation and dimension process (arrowed line: residual vector, dot line: bracing members, blue and red line: compression and tension member)

Balancing architectural aesthetics with constraints on structural requirements, six square wooden frames with a 3.6m side length were hung on the tube at six different heights, with deviation rings in place. These square frames connected the core tube by extending four sides of the rectangular ring until they meet the outer frame. The outer frame is also designed to have an 8cm x 8cm cross-sectional dimension.

Karamba3D was again used to verify the system's serviceability. The added outer frame was considered as a beam element (fixed connection) and was located on the hinged core tube. As Figure 15 indicates, the maximum displacement reached 10.81cm, which occurred at the hanging corner on the top frame, as shown in green color. Displacement of each bar element ranged from 0 to 9.88 cm, which was colored gradually from white to magenta. The displacement is within acceptable limits.

Considering the types of existing processed timber products and saving more structural safety redundancy, four different sectional sizes of 8X8cm, 10X8cm, 10X10cm, and 12X12cm were arranged for each element. To convey a design concept of material reusability, the squared timber members in the two reinforced stories were replaced with wooden logs. Three months after the construction of the wooden tower, deformation was precisely as the analysis results predicted (Figure 16). Further joint design, robotic milling, and assembling process will be presented in other works.

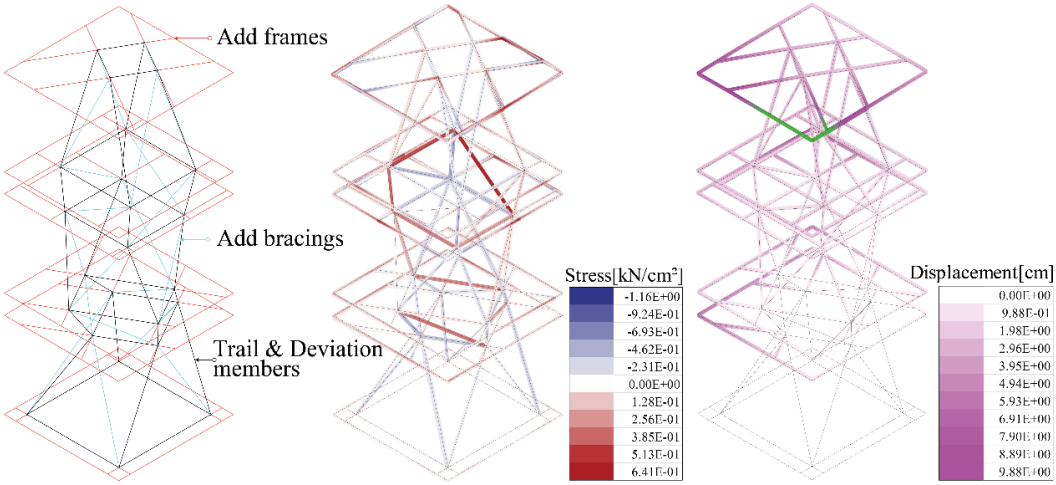


Figure 15: Finite element analysis for the whole structure

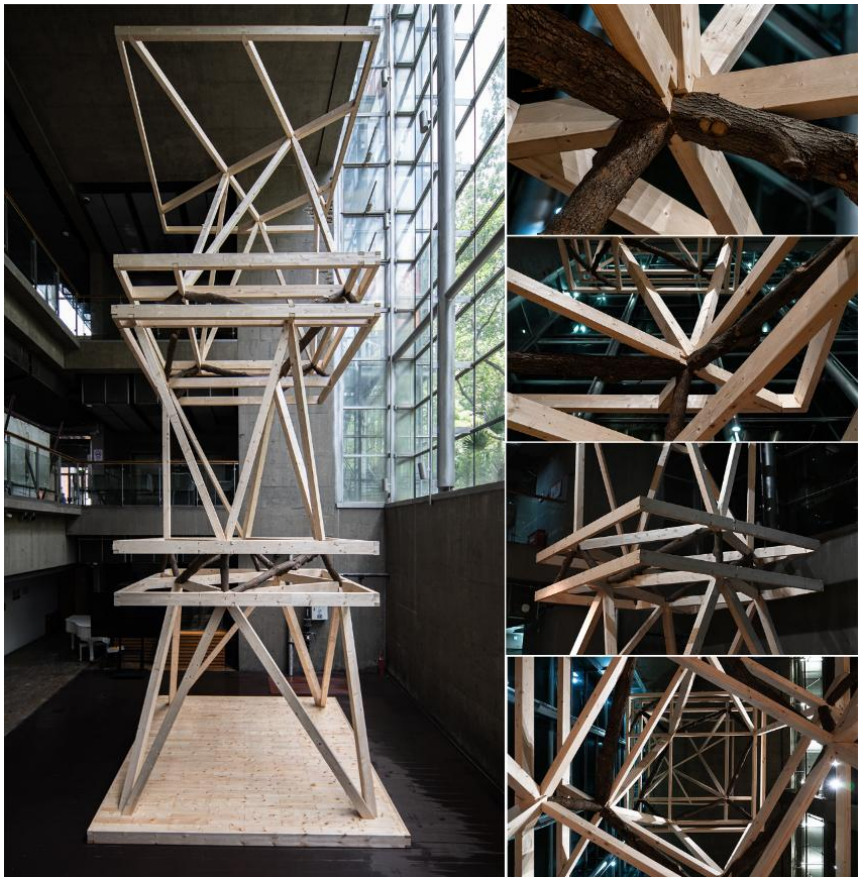


Figure 16: Built a wooden tower

4. Conclusion and Improvement

This article presents an equilibrium-based design workflow for Member Structural System integrating CEM, VGS, and Material concretization. The advantages of this method are as follows:

1. Contrary to many structures that need a complicated post optimization process, the proposed workflow considers equilibrium a priori during the form-finding and transformation process; the generated geometry with minimized load path means the designed structure is naturally efficient.
2. In contrast to the opaque nature of traditional structural analysis, this workflow empowers architects with direct, interactive agency in the design process. This interactive capability bridges the gap between qualitative, design-led decision-making and quantitative, performance-driven goals.
3. The workflow enables further refinement of the strut-tie model, providing the critical size of the cross-section. It addresses the material concretization problem, which conceptual design tools, such as CEM and VGS, are unable to solve.

Besides the meaningful aspects, deficiencies of current research also have to be improved in the future.

1. Current optimization methods for equilibrium geometry models generated via CEM remain inefficient, characterized by excessive iterations and high computational costs. Future research could leverage gradient-based automatic differentiation to identify optimal load path topologies.
2. The force diagram generated by VGS yields a cluster, especially on a 3D complex spatial network, which is hard to recognize; it causes difficulty in transforming the force diagram to achieve a specific design goal.

3. In addition to determining the critical cross-sectional dimensions, methods for optimizing the sizes of all members within the system should be identified, and the global stability issue remains to be thoroughly investigated.

5. Image Credits

Figure 12 was downloaded from Wikimedia Commons: https://en.wikipedia.org/wiki/Pagoda_of_Fogong_Temple#/media/File:Pagodaoffogongtemple2019.jpg. Jiang Xinchen and Xie Xinjie photographed Figure 16. The first author drew others.

6. Funding

This work was supported by the China-Belgium (Wallonia) Inter-governmental Science and Technology Cooperation Project: Research on Wooden Green Building System based on the Coupling of Graphic Statics Design Method and Robotic Fabrication Technology (Grant No. 2022YFE0141400, National Key Research and Development Program of China).

7. References

Akbarzadeh M. (2016). *3D Graphical Statics using 3D Reciprocal Diagrams*. Ph.D. thesis, ETH Zürich, Zürich, Switzerland.

Aurelio Muttoni, Joseph Schwartz, Bruno Thürlimann. (1997). *Design of concrete structures with stress fields.* Boston : Birkhäuser, Basel.

Bow R. (1873). *Economics of Construction in Relation to Framed Structures.* E. and F.N. Spon, London. https://doi.org/10.1017/CBO9781107297005

Barnes M. R. (1999). Form Finding and Analysis of Tension Structures by Dynamic Relaxation. *International Journal of Space Structures* 14(2), 89 – 104.

Baker W.F., Beghini L.L., Mazurek A. et al. (2013). Maxwell's reciprocal diagrams and discrete Michell frames. Struct Multidisc. Optim. 48, 267 – 277. https://doi.org/10.1007/s00158-013-0910-0

Calladine C.R., Pellegrino S. (1991). First-order infinitesimal mechanisms. *International Journal of Solids and Structures* 27(4), 505–515. https://doi.org/10.1016/0020-7683(91)90137-5

Clemens Preisinger, Moritz Heimrath. (2014). Karamba—A Toolkit for Parametric Structural Design. *Structural Engineering International*, 24:2, 217–221. https://doi.org/10.2749/101686614X13830790993483

Crapo H. (1979). Structural rigidity. *Structural Topology* (1), 26–45, 73. http://hdl.handle.net/2099/521

Cremona L. (1890). *Graphical Statics: Two Treatises on the Graphical Calculus and Reciprocal Figures in Graphical Statics.* Oxford: Clarendon Press.

Culmann K. (1864). *Die Graphische Statik (1st ed.).* Zürich: Verlag Meyer und Zeller.

D. Veenendaal & P. Block (2012). An overview and comparison of structural form-finding methods for general networks. *International Journal of Solids and Structures*, 49(26), 3741 – 3753. https://doi.org/10.1016/j.ijsolstr.2012.08.008

D'Acunto P., et al. (2019). Vector-based 3D graphic statics: a framework for the design of spatial structures based on the relation between form and forces. *Int J Solids Struct* 167, 58–70. https://doi.org/10.1016/j.ijsolstr.2019.02.008

D'Acunto Pierluigi, Jasienski Jean-Philippe, Ohlbrock Patrick Ole & Fivet Corentin (2017). Vector-Based 3D Graphic Statics: Transformations of Force Diagrams. IASS Annual Symposium 2017 "*Interfaces: architecture, engineering, science*" At: Hamburg.

Fivet, C. (2016). Projective transformations of structural equilibrium. *International Journal of Space Structures*, 31(2-4), 135–146. 10.1177/0266351116660796

Jasienski, J. P., Shen, Y., Ohlbrock, P. O., Zastavni, D., & d'Acunto, P. (2024). A computational implementation of Vector-based 3D Graphic Statics (VGS) for interactive and real-time structural design. *Computer-Aided Design*, 171, 103695. https://doi.org/10.1016/j.cad.2024.103695

James Gere & Barry J. Goodno (2016). *Mechanics of Materials, 9th edition*, CL Engineering.

Kilian, A. & Ochsendorf, J. (2005). Particle-spring systems for structural form finding. *Journal of the International Association for Shell and Spatial Structures.* 46. 77–84.

Konstantatou, M., P. D'Acunto, & A. McRobie (2018). Polarities in structural analysis and design: n-dimensional graphic statics and structural transformations. *International Journal of Solids and Structures* 152–153, 272–293. https://doi.org/10.1016/j.ijsolstr.2018.07.003

Lee, J. (2018). *Computational Design Framework for 3D Graphic Statics.* Ph.D. thesis, ETH Zürich, Zürich, Switzerland.

Masoud Akbarzadeh, Tom Van Mele, Philippe Block. (2015). On the equilibrium of funicular polyhedral frames and convex polyhedral force diagrams, *Computer-Aided Design* 63, 118–128. https://doi.org/10.1016/j.cad.2015.01.006.

Maxwell, J. C. (1864). On reciprocal figures and diagrams of forces. *Philosophical Magazine Series* 4 27(182), 250–261. https://doi.org/10.1080/14786446408643663

Maxwell, J. C. (1870). On reciprocal figures, frames, and diagrams of forces. *Transactions of the Royal Society of Edinburgh* 26(1), 1–40. https://doi.org/10.1017/S0080456800026351

Micheletti, A. (2008). On generalized reciprocal diagrams for self-stressed frameworks. *International Journal of Space Structures* 23 (3), 153–166. 10.1260/026635108786260974

Ohlbrock P. O., Schwartz, J. (2016). Combinatorial equilibrium modeling. *International Journal of Space Structures* 31(2–4), 177–89. 10.1177/0266351116660799

Ohlbrock Patrick Ole, Pierluigi D'Acunto. (2020). A Computer-Aided Approach to Equilibrium Design Based on Graphic Statics and Combinatorial Variations. *Computer-Aided Design*121(4), 102802. https://doi.org/10.1016/j.cad.2019.102802

Oakley, D. R., & Knight, N. F. (1995). Nonlinear structural response using adaptive dynamic relaxation. (NASA Technical Memorandum 109132).

Preisinger, C. (2013). Linking Structure and Parametric Geometry. *Archit Design* 83: 110–113. https://doi.org/10.1002/ad.1564

Piker, D. (2013). Kangaroo: Form Finding with Computational Physics. *Archit Design*, 83: 136–137. https://doi.org/10.1002/ad.1569

Rankine, W. (1864). Principle of the equilibrium of polyhedral frames. *Philosophical Magazine Series* 4 27(180), 92. https://doi.org/10.1080/14786446408643629

Rankine, W.J.M. (1858). *A Manual of Applied Mechanics.* Richard Griffin and Company, Glasgow.

Saad, Y. (2003). *Iterative methods for sparse linear systems*. Society for Industrial and Applied Mathematics.

Rutten David. (2013). Galapagos: On the Logic and Limitations of Generic Solvers. *Architectural Design, 83*, 132–135.

Tutte, W. T. (1963). *"How to draw a graph"*, Proceedings of the London Mathematical Society, Third Series, 13: 743–767.

Van Mele, T., L. Lachauer, M. Rippmann, and P. Block. (2012). Geometry-based understanding of structures. *Journal of the International Association for Shell and Spatial Structures* 53(174), 285–295.
Waclaw Zalewski & Edward Allen. (1998). *Shaping Structures: statics.* Wiley, New York.
Whitney, H. (1933). Planar graphs. *Fund. Math.* 21, 73–84. http://eudml.org/doc/212650
Yao Lu, Márton Hablicsek, Masoud Akbarzadeh. (2024). Algebraic 3D Graphic Statics with Edge and Vertex Constraints: A Comprehensive Approach to Extend the Solution Space for Polyhedral Form-Finding. *Computer-Aided Design* Volume 166, 103620. https://doi.org/10.1016/j.cad.2023.103620
Zongshuai Wan, Patrick Ole Ohlbrock, Pierluigi D'Acunto, Zhenggang Cao, Feng Fan, Joseph Schwartz. (2021). A form-finding approach for the conceptual design of air-supported structures using 3D graphic statics. *Computers & Structures.* Volume 243.
https://doi.org/10.1016/j.compstruc.2020.106401